



RESEARCH ARTICLE | SEPTEMBER 01 2023

Data-driven stochastic spectral modeling for coarsening of the two-dimensional Euler equations on the sphere

Sagy R. Ephrati ; Paolo Cifani; Milo Viviani ; Bernard J. Geurts



Physics of Fluids 35, 096601 (2023)

<https://doi.org/10.1063/5.0156942>



View
Online



Export
Citation

CrossMark

Articles You May Be Interested In

Determination of bittering substance and phytochemical compositions of gesho (*Rhamnus Prinoides*) grown in Ethiopia

AIP Conference Proceedings (June 2023)

Interface retaining coarsening of multiphase flows

Physics of Fluids (July 2021)

Coarsening kinetics in demixed lead borate melts

J. Chem. Phys. (June 2013)



APL Quantum
Bridging fundamental quantum research with technological applications

Now Open for Submissions
No Article Processing Charges (APCs) through 2024

Submit Today



Data-driven stochastic spectral modeling for coarsening of the two-dimensional Euler equations on the sphere

Cite as: Phys. Fluids **35**, 096601 (2023); doi: 10.1063/5.0156942

Submitted: 4 May 2023 · Accepted: 10 August 2023 ·

Published Online: 1 September 2023



View Online



Export Citation



CrossMark

Sagy R. Ephrati,^{1,a)}  Paolo Cifani,¹ Milo Viviani,²  and Bernard J. Geurts^{1,3}

AFFILIATIONS

¹Mathematics of Multiscale Modeling and Simulation, Faculty EEMCS, University of Twente, 7500 AE Enschede, The Netherlands

²Scuola Normale Superiore di Pisa, 56126 Pisa, Italy

³Multiscale Energy Physics, CCER, Faculty Applied Physics, Eindhoven University of Technology, 5600 MB Eindhoven, The Netherlands

^{a)}Author to whom correspondence should be addressed: s.r.ephrati@utwente.nl

ABSTRACT

A resolution-independent data-driven subgrid-scale model in coarsened fluid descriptions is proposed. The method enables the inclusion of high-fidelity data into the coarsened flow model, thereby enabling accurate simulations also with the coarser representation. The small-scale model is introduced at the level of the Fourier coefficients of the coarsened numerical solution. It is designed to reproduce the kinetic energy spectra observed in high-fidelity data of the same system. The approach is based on a control feedback term reminiscent of continuous data assimilation implemented using nudging (Newtonian relaxation). The method relies solely on the availability of high-fidelity data from a statistically steady state. No assumptions are made regarding the adopted discretization method or the selected coarser resolution. The performance of the method is assessed for the two-dimensional Euler equations on the sphere for coarsening factors of 8 and 16 times. Applying the method at these significantly coarser resolutions yields good results for the mean and variance of the Fourier coefficients and leads to improvements in the empirical probability density functions of the attained vorticity values. Stable and accurate large-scale dynamics can be simulated over long integration times and are illustrated by capturing long-time vortex trajectories.

© 2023 Author(s). All article content, except where otherwise noted, is licensed under a Creative Commons Attribution (CC BY) license (<http://creativecommons.org/licenses/by/4.0/>). <https://doi.org/10.1063/5.0156942>

I. INTRODUCTION

Two-dimensional incompressible hydrodynamics models are fundamental for studying physical phenomena in atmospheric and oceanic flows. Typical examples include the two-dimensional Euler equations, quasi-geostrophic (QG) equations, and (rotating) shallow water equations. A characteristic feature of these flows is the formation of both large vorticity structures through the inverse energy cascade and small-scale vorticity filaments through the enstrophy cascade.¹ In the absence of large-scale dissipation, energy accumulates in the lowest wavenumbers, which leads to large-scale energy condensates.² An understanding of such large-scale structures finds meaningful applications in geophysical flows, which are often dominated by large vortices.³ This leads to an energy spectrum with two scaling laws, where the large scales follow a scaling steeper than $l^{-5/3}$ often observed in two-dimensional turbulence³ and the small-scale energy is distributed following an l^{-1} scaling.² These energy spectra are often compared to

the Nastrom–Gage kinetic energy spectrum at the atmospheric meso-scale.⁴ In realistic conditions, the energy spectrum extends over several orders of magnitude, making it computationally infeasible to fully resolve all scales that are present in the flow. Simplifications are required, either by reducing the complexity of the underlying mathematical model⁵ or by reducing the spatial or temporal resolution with which the dynamics are resolved.⁶ In this paper, we will focus on high-fidelity coarsening of the two-dimensional Euler equations on the sphere by applying an *online/offline* approach to obtain accurate coarse-grained numerical solutions of statistically steady states. In particular, explicit information on well-resolved dynamics is obtained from high-resolution simulations in the offline phase, which is applied in an online control feedback model for accurate coarse-grained simulations.

There is considerable interest in achieving accurate numerical solutions of fluid flows at reduced computational costs.⁷ This forms

the main challenge of large eddy simulation (LES), which aims to provide skillful large-scale predictions of complex flows by numerically solving spatially filtered momentum equations. The filter may be defined explicitly by the user, typically by imposing a filter width Δ that decomposes the prognostic variables into filtered large-scale and residual small-scale components. The filter can also be defined implicitly by applying discrete operators on coarse computational grids.^{8,9} Often, a model term is included to compensate for unresolved dynamics due to coarsening to retain a sufficiently detailed description of turbulent flows at high Reynolds numbers.^{10–14} Coarsening can also implicitly provide this model term, which is embraced in implicit LES.^{15,16} Implicit LES aims for high-fidelity coarsening by using the truncation error of the numerical approximations, in the form of numerical dissipation, in place of an explicitly defined turbulence model. Recent studies have shown that under-resolved model-free simulations yield good numerical results at reduced computational costs in, e.g., turbulent boundary layers¹⁷ and industrial flow problems,¹⁸ and are supported by analysis of the dispersion and diffusion effects owing to the underlying discretization.^{19,20}

The growing availability of computational resources has facilitated the use of high-resolution direct numerical simulations (DNS) as a source of data from which coarse-grid fluid models may be derived.²¹ Data-driven LES methods have successfully been developed in recent years, for example, by using neural networks to compute a variable eddy viscosity⁸ to approximate a reference kinetic energy spectrum²² or to model subgrid scale-scale forces.²³ Other approaches have focused on learning subgrid-scale models using as few tunable parameters as possible,²⁴ leading to accurate models for selected quantities of interest. Alternatively, approaches based on interpolation of small high-resolution patches of the spatial domain^{25–27} and data-driven residual modeling via global basis functions²⁸ have also shown computational efficiency and accuracy in coarse-grained numerical solutions.

Data assimilation provides an alternative method to achieve accurate coarse-grained results by combining predictions with real-time observations. In continuous data assimilation (CDA), observational data are incorporated into the prediction, while the numerical model is being integrated in time.^{29–31} Specifically, the difference between the numerical prediction and the corresponding observation determines a nudging term that is added to the governing equations. Studies on nudging of dissipative fluid models have shown that a range of nudging strengths may be chosen that all yield an accurate coarse-grained representation of the true solution.^{29,32,33} Adaptive nudging strengths based on energy balance have also been proposed³⁴ resulting in faster convergence toward the reference compared to a simulation that exploits a constant nudging strength. Data assimilation methods also benefit from reduced computational costs of forecasting geophysical quantities. This can be achieved, for example, by forecasting time series using long short-term memory neural networks.³⁵ In this paper, we achieve computational cost reduction by combining coarse numerical discretization with a data-driven model term to compensate for coarsening effects, inspired by data assimilation algorithms. Since data assimilation methods often rely on observational data to achieve high-fidelity coarsened solutions, the uncertainty originating from measurement errors has to be taken into account, as well as possible accumulation of discretization errors.³⁶

Models of geophysical fluid flows often employ stochasticity as a means to model uncertainty inherent to flows.³⁷ Uncertainty arises

predominantly from differences in initial conditions, errors in measurements, and model incompleteness. Low-dimensional models describing qualitative features of geophysical fluid flows often serve as a test bed for stochastic forcing. For example, stochastic forcing based on subgrid data in the two-scale Lorenz '96 system resulted in improved forecasting skill compared to deterministic parametrizations.³⁸ The use of stochasticity also extends to describing experimental findings. For example, evidence has been provided that the large-scale motion in fully developed turbulent swirling flow can be accurately described by a low-dimensional stochastic system.³⁹ Similarly, a recent study⁴⁰ uses a low-dimensional system with stochastically perturbed dynamics to represent the processes underlying laboratory earthquake experiments. In these studies, the inclusion of stochasticity allowed for recovering quantitative properties of the observed systems. Ultimately, the exact way in which stochasticity is included in numerical simulations remains a modeling choice and may lead to qualitatively different effects on the dynamics.⁴¹ These approaches have also been applied successfully to more complete geophysical models. Examples include the modeling of uncertainty through Casimir-preserving stochastic forcing for the two-dimensional Euler equations^{42–45} and energy-preserving stochastic forcing in the quasi-geostrophic equations⁴⁶ and rotating shallow water equations.⁴⁷ An alternative approach is based on statistics of subgrid data that lead to a stochastic forcing and eddy viscosity, which has been applied to the barotropic vorticity equation on the sphere.⁴⁸ This approach was found to accurately model uncertainty and produce energy spectra on coarse computational grids that closely match reference high-fidelity simulations at much higher resolutions.

In this paper, we propose an *online* data-driven standalone stochastic model for coarse numerical simulations of statistically steady states of the two-dimensional Euler equations on the sphere. Data of a statistical equilibrium are extracted from an *offline* high-resolution precursor simulation in the form of statistics of coefficients of spherical harmonic modes and are included as a stochastic forcing term following the formulation of the continuous-time limit of the 3D-Var algorithm⁴⁹ as presented in Ref. 50. Here, however, the parameters of the forcing are determined heuristically and solely from the high-resolution data and do not require additional explicit tuning, hence leading to a data-driven model that requires few tunable parameters. The parameter values do not follow from a minimization problem; therefore, the proposed method does not constitute a variational data assimilation method. Rather, a modeling term is added to the coarsened numerical simulation based on these *a priori* collected data, similar to data-driven LES. This term models the unresolved interactions between the modes as a linear stochastic process for each spherical harmonic coefficient separately and is designed to reproduce the energy spectrum of the high-resolution simulation. Like CDA, the model term is included as a feedback control term. This term nudges the coarse grid solution toward an *a priori* measured statistically steady state, leading to a standalone model that does not require additional measurements during a simulation. We opt for the nudging strength to be equal to the inverse of the characteristic timescale of the corresponding spherical harmonic mode. This choice has the benefit that it mimics the measured temporal correlation. The nudging procedure is performed via a prediction–correction scheme in which we first fully complete a time integration step involving all true fluxes and subsequently we apply the nudge as a correction to the predicted solution.

This results in straightforward implementation in existing computational methods and leads to a numerical scheme of the same form as the diagonal Fourier domain Kalman filter^{51,52} with prescribed gain. Striking features of the high-fidelity reference solution were captured in the coarser model using this stochastic model.

The paper is structured as follows. The two-dimensional Euler equations and the adopted numerical method are introduced in Sec. II. In Sec. III, we describe the model and focus, in particular, on how the model parameters are specified. In Sec. IV, we define the reference solution and apply the model at two coarse resolutions. The results are assessed qualitatively and by means of statistics of Fourier coefficients. Subsequently, we show that the model is capable of reproducing large-scale vortex dynamics of the reference solution. Section V concludes the paper and suggests directions for further research.

II. GOVERNING EQUATIONS AND NUMERICAL METHODS

The model that will be studied in this work is given by the two-dimensional Euler equations on the unit sphere \mathbb{S}^2 . These equations arise as the two-dimensional Navier–Stokes equations in the inviscid limit and describe vortex dynamics.¹ In fact, the Euler equations belong to a larger family of two-dimensional geophysical fluid models that may be derived from a variational point of view.^{5,53} Starting from the rotating shallow water equations, the quasi-geostrophic (QG) equations and the Euler equations can be derived from a sequence of simplifying assumptions. The QG equations are derived in a regime where a balance between rotation and pressure exists.⁵⁴ The Euler equations instead follow by discarding effects induced by rotation and the free surface. In addition, the Euler equations do not allow for inhomogeneous effects in the vertical direction. The dynamics are given in streamfunction-vorticity formulation by

$$\dot{\omega} = \{\psi, \omega\} = \frac{1}{\cos \phi} \left(\frac{\partial \psi}{\partial \phi} \frac{\partial \omega}{\partial \theta} - \frac{\partial \psi}{\partial \theta} \frac{\partial \omega}{\partial \phi} \right), \quad (1)$$

$$\Delta \psi = \omega.$$

Here, ω is the vorticity, ψ is the streamfunction, and $\{\cdot, \cdot\}$ is the Poisson bracket. The latitude is denoted by ϕ and ranges from $\pi/2$ at the north pole to $-\pi/2$ at the south pole, and the longitude is denoted by θ and ranges from 0 to 2π . The vorticity and the streamfunction are related via the Laplace operator Δ . The vorticity relates to the fluid velocity \mathbf{v} via $\omega = \text{curl } \mathbf{v}$. These equations are part of a larger family of geophysical fluid models that can be derived from a variational principle and inherently reflect particular conservation laws.⁵³ The governing equation (1) form a Lie–Poisson system⁵⁵ with a Hamiltonian \mathcal{H} and an infinite number of conserved quantities, known as Casimirs \mathcal{C}_k , given by

$$\mathcal{H}(\omega) = -\frac{1}{2} \int \omega \psi, \quad (2)$$

$$\mathcal{C}_k(\omega) = \int \omega^k, \quad k = 1, 2, \dots, \quad (3)$$

where the integral is taken over the spatial domain.

A discrete system with a similar Lie–Poisson structure is obtained after so-called geometric quantization. This structure-preserving discretization is based on a finite truncation of the Poisson bracket, as proposed in Refs. 56 and 57, and rests on the

theory of quantization.^{58–60} First, an $N > 1$ is chosen, which can be thought of as the numerical resolution. Subsequently, a total of $\frac{N(N+1)}{2} - 1$ global basis functions are determined explicitly before carrying out a simulation. These functions serve to construct the discrete vorticity representation W . A finite-dimensional approximation of the system (1) is obtained as

$$\dot{W} = [P, W], \quad (4)$$

$$\Delta_N P = W.$$

Here, W is the vorticity matrix, P is the stream matrix, and $W, P \in \mathfrak{su}(N)$, that is, skew-Hermitian, traceless $N \times N$ matrices.

The discrete system (4) is interpreted as follows. A continuous vorticity field ω on the sphere can be expanded in a spherical harmonic basis $\{Y_{lm}\}$ as $\omega = \sum_{l,m} c_{lm} Y_{lm}$. The spherical harmonic coefficients c_{lm} are used to construct the matrix W . Namely,

$$W = \sum_{l=0}^{N-1} \sum_{m=0}^l c_{lm} T_{lm}^N. \quad (5)$$

Here, $\{T_{lm}^N\}$ is the so-called quantized spherical harmonic basis,⁶¹ which provides a particular discrete approximation to the spherical harmonic basis $\{Y_{lm}\}$. The quantized system is obtained by applying a projection Π_N from the smooth functions on the sphere to the skew-Hermitian $N \times N$ matrices.⁶¹ The projection is constructed such that for $N \rightarrow \infty$ and two smooth functions f, g , the following properties hold:

$$\Pi_N f - \Pi_N g \rightarrow 0 \text{ implies } f = g, \quad (6)$$

$$\Pi_N \{f, g\} = \frac{N^{3/2}}{\sqrt{16\pi}} [\Pi_N f, \Pi_N g] + \mathcal{O}(1/N^2). \quad (7)$$

That is, this provides a second-order accurate discretization of the dynamics. In fact, the quantized representation enables the structure-preserving discretization.^{57,62} The basis element T_{lm}^N is a sparse skew-Hermitian traceless matrix, nonzero only on the m th sub- and superdiagonal. We refer to Ref. 61 for a detailed description of the quantized basis. The quantized Laplacian Δ_N can be derived as a complicated expression, given in Ref. 63. The matrix P then follows by applying the inverse quantized Laplacian to W . The bracket $[P, W] = PW - WP$ is the standard matrix commutator. In the limit of $N \rightarrow \infty$, the structure constants of the Lie algebra $\mathfrak{su}(N)$ converge to those of $C^\infty(\mathbb{S}^2)$ expressed in terms of spherical harmonics. This convergence implies that smooth functions on the sphere can be approximated by finite-dimensional matrices by means of Eq. (5).⁶¹

The discrete system is a Lie–Poisson system with a Hamiltonian H and N conserved quantities C_k ,

$$H(W) = \frac{1}{2} \text{Tr}(PW), \quad (8)$$

$$C_k(W) = \text{Tr}(W^k), \quad k = 1, \dots, N. \quad (9)$$

Equation (4) is solved numerically using the second-order isospectral midpoint rule,^{64,65} using the parallelized implementation described in Ref. 61. This is a Lie–Poisson integrator, conserving the N discrete Casimir functions exactly. Given a time step size h , a time integration step proceeds as follows:

$$\begin{aligned}
 W_n &= \left(I - \frac{h}{2} \Delta_N^{-1} \tilde{W} \right) \tilde{W} \left(I + \frac{h}{2} \Delta_N^{-1} \tilde{W} \right), \\
 W_{n+1} &= \left(I + \frac{h}{2} \Delta_N^{-1} \tilde{W} \right) \tilde{W} \left(I - \frac{h}{2} \Delta_N^{-1} \tilde{W} \right),
 \end{aligned}
 \tag{10}$$

i.e., given W_n the intermediate solution \tilde{W} is obtained first, after which W_{n+1} is determined to complete a time step.

An example of the Euler equations integrated at high resolution using (10) is given in Fig. 1. This figure shows the vorticity fields as Hammer projections in order to display the entire spherical domain. The different stages of the vorticity evolution of a high-resolution numerical simulation are shown before reaching a statistically steady state. From a smooth initial condition where energy is distributed only in large-scale modes (top left panel), the vorticity field undergoes a period of vorticity mixing (top right and bottom left panels) where energy is distributed across the available spatial scales. Finally, it reaches a statistically steady state (bottom right panel) in which the energy spectrum does not undergo any qualitative changes and the large-scale vorticity structures persist. The flow dynamics reveal that large-scale low-dimensional structures are present in the vorticity field at late times.⁶⁶ This motivates the use of coarse computational grids to capture the dynamics in the asymptotic time regime.

To compare numerical solutions at different resolutions, we define a fine-to-coarse filter. Throughout the paper, the applied filter is a spectral cutoff filter, setting all coefficients corresponding to a wavenumber larger than a specified wavenumber to zero. In the following, we consistently choose a cutoff wavenumber defined by the coarse-grid resolution, which yields a filtered solution containing only spatial scales resolvable on the corresponding coarse grid.

Significantly decreasing the resolution yields a qualitatively different statistically steady state, as shown in Fig. 2. Illustrated is a snapshot of the fine-grid solution ($N = 512$), a filtered version thereof (only the components up to $N = 64$ are shown), and a snapshot of a coarse-grid solution ($N = 64$) using the algorithm as outlined in (10). These simulations are initialized using the smooth vorticity field in Fig. 1. High-frequency components are visible in the snapshot of the high-resolution numerical solution, which develop as a result of the enstrophy cascade. By applying a spectral cutoff filter to the fine numerical solution, we obtain a smooth vorticity field. By definition of the filter, this field can be fully resolved using the coarse resolution. Since the filtered fine solution is an orthogonal projection onto the coarse-resolvable subspace of solutions, it defines the best attainable result on the coarse grid and the result is a description of the large-scale components of the flow, influenced by all fine-grid resolvable scales.

A clear qualitative difference exists between the filtered high-resolution vorticity and the vorticity obtained at a lower resolution, which is best explained by analyzing the energy spectra. Two-dimensional systems without large-scale dissipation allow for energy accumulation in the lowest wavenumbers, leading to large-scale vorticity structures.³ These so-called condensates contain most of the energy of the system and result in an energy spectrum steeper than the $l^{-5/3}$ scaling typically observed in the large scales of two-dimensional turbulence. Here, we observe a scaling of roughly $l^{-9/4}$ following from the randomly chosen initial condition. The energy in the small scales is distributed according to a l^{-1} scaling also observed in other studies.^{2,66} The energy spectrum of the coarse numerical solution deviates from the spectrum of the fine numerical solution at the smallest resolvable scales. Nonetheless, the energy in the large scales is captured well. Additionally, the energy decay at large wavenumbers follows the same

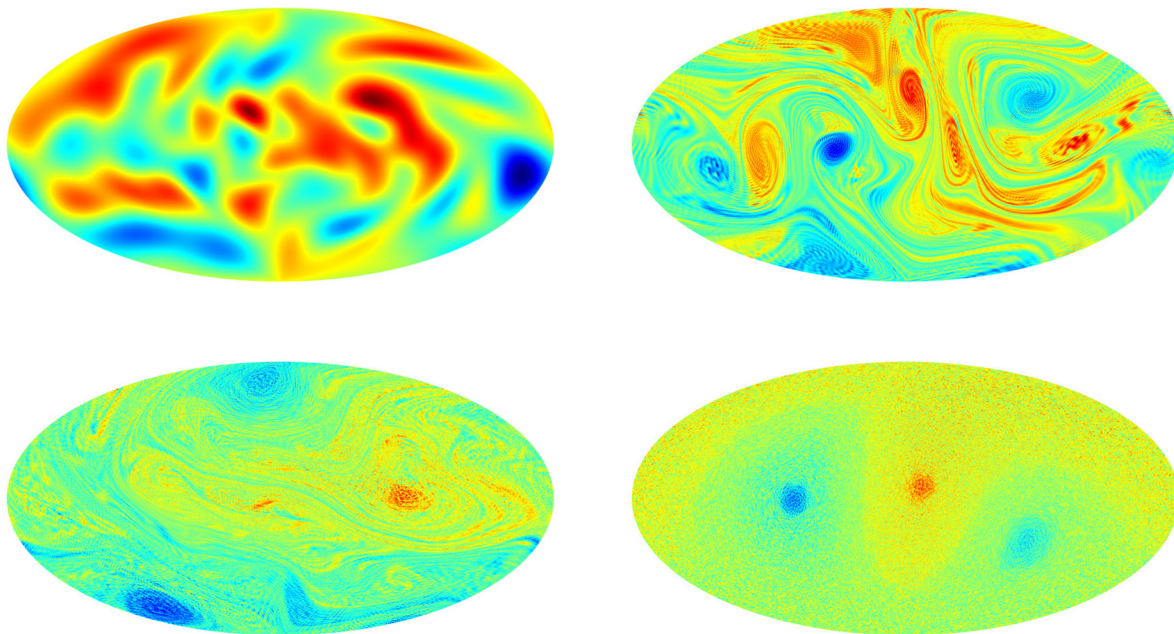


FIG. 1. Snapshots of a high-resolution ($N = 512$) numerical simulation of system (4). The vorticity field is initialized as a random large-scale field (top left), after which it undergoes a period of vorticity mixing (top right, bottom left) before reaching a statistically steady state in which large-scale vorticity structures dominate the solution (bottom right).

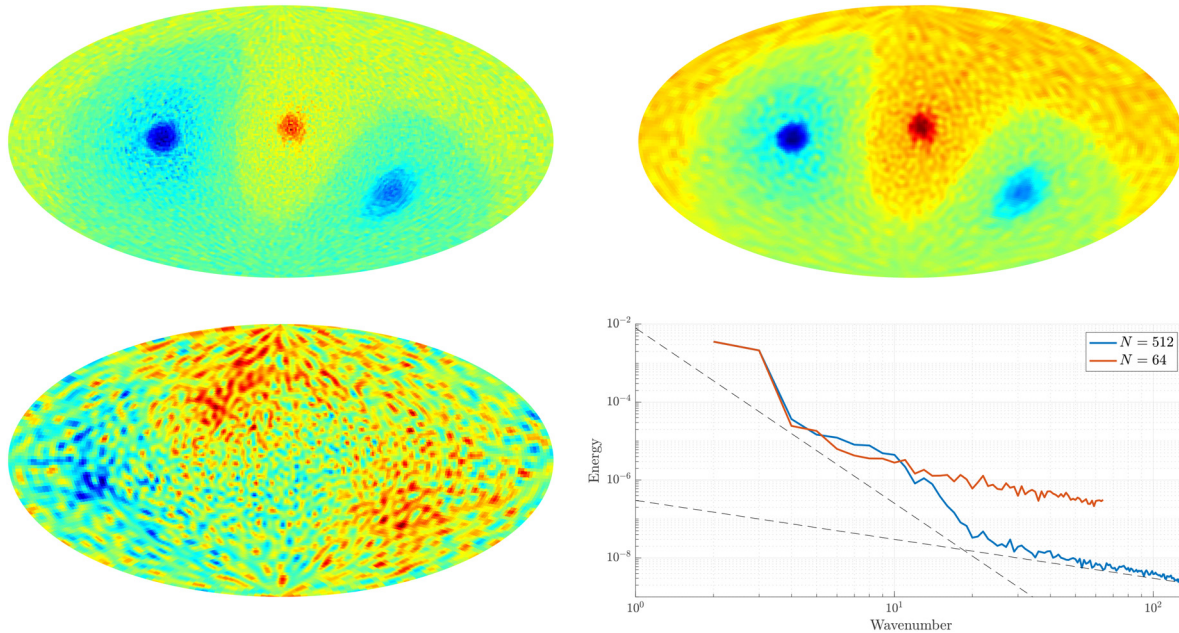


FIG. 2. Snapshots of the fine vorticity field (top left), a filtered version thereof (top right), and a coarse vorticity field (bottom left) after reaching a statistically steady state. The energy spectra of the fine and coarse fields are shown in the bottom right panel.

decay of l^{-1} as observed in the high-resolution result, where l is the wavenumber. Despite this agreement, the instantaneous vorticity field at the coarse resolution differs significantly from the high-resolution result. The increased energy in high-frequency modes of the coarse numerical solution causes the small scales to dominate the vorticity field observed in Fig. 2. We note that the energy spectrum of the filtered reference solution exactly coincides with the spectrum of the reference solution until the cutoff frequency at wavenumber 64, by definition of the filter. The discrepancy between the energy levels of the coarse numerical solution and the filtered reference may, therefore, be reduced by an appropriate forcing term. In Sec. III, we introduce a data-driven forcing term that yields the desired energy level at each frequency and thus regularizes the numerical solution.

III. DATA-DRIVEN SPECTRUM-PRESERVING FORCING

In Sec. II, we observed that a qualitative difference exists between the statistical steady states obtained at low and high resolutions. One of the defining features of a statistically steady state is its kinetic energy spectrum. The corresponding energy spectra of the solutions reveal a considerable difference between the energy levels of the small scales present in the flow. The discrepancy between the spectra may be reduced by introducing an appropriate forcing or correction term to the coarse numerical simulations. In a statistically steady state, the spectrum is fully described using the mean and variance of the magnitude of the spectral coefficients in the statistically steady state. Therefore, the goal of the model is to reproduce these quantities accurately and, in doing so, recover the reference kinetic energy spectrum. In this section, we describe a forcing that achieves this goal, particularly in situations where the number of modes is kept low. For this purpose, we opt for a model that aims to match the mean and variance

of the coefficient magnitudes to reference values. This approach is based on reference data corresponding to independently obtained highly resolved direct numerical simulations aiming to combine computational feasibility with accurate flow predictions. The model derivation consists of three steps, being the modal expansion of the dynamics, the formulation of the forcing term, and the definition of the forcing parameters.

A. Modal expansion of the dynamics

To define the spectral forcing, we first expand the vorticity in the spherical harmonics basis functions. We provide these details for the continuous system and the quantized system.

In the continuous system, the basis coefficients c_{lm} are obtained by projecting the vorticity ω on the basis coefficients using the inner product of the sphere. For two smooth functions g, h , we define the inner product $\langle g, h \rangle$ as

$$\langle g, h \rangle = \int_{\phi=-\pi/2}^{\pi/2} \int_{\theta=0}^{2\pi} g(\phi, \theta) h(\phi, \theta)^* \cos \phi \, d\theta d\phi, \quad (11)$$

where $*$ denotes the complex conjugate. The spherical harmonic coefficients and their evolution are consequently defined as

$$c_{lm} = \langle \omega, Y_{lm} \rangle, \quad (12)$$

$$\dot{c}_{lm} = \langle \dot{\omega}, Y_{lm} \rangle = \langle \{\psi, \omega\}, Y_{lm} \rangle. \quad (13)$$

The quantized system relies on discrete representations T_{lm}^N of the spherical harmonics. These are skew-symmetric matrices, and therefore, we adopt the Frobenius inner product for projection onto the quantized basis. Given two skew-Hermitian matrices G, H , we define

$$\langle G, H \rangle_F = \text{Tr}(G^* H), \tag{14}$$

where $*$ denotes the conjugate transpose. We compute the basis coefficients and their evolution via

$$\begin{aligned} c_{lm} &= \langle W, T_{lm}^N \rangle_F, \tag{15} \\ \dot{c}_{lm} &= \langle \dot{W}, T_{lm}^N \rangle_F = \langle [P, W], T_{lm}^N \rangle_F := L(\mathbf{c}, l, m). \tag{16} \end{aligned}$$

Further expanding (13) and (16) leads to complicated expressions and is, in fact, not necessary. Instead, only the projections (12) and (15) are required, as well as the reconstruction of the vorticity field from the basis coefficients via a linear combination. We note that other choices of basis functions are also possible for the projection and subsequent forcing, e.g., proper orthogonal decomposition (POD) modes may be adopted for this purpose.⁶⁷ In what follows, we consider the quantized system and the corresponding projection onto the basis $\{T_{lm}^N\}$.

Having defined the basis coefficients, we expand the vorticity matrix in the quantized spherical harmonic basis $\{T_{lm}^N\}$,

$$W(t) = \sum_{l=0}^{N-1} \sum_{m=0}^l c_{lm}(t) T_{lm}^N. \tag{17}$$

The energy in solution components at index l is then defined as

$$E_l(t) = \frac{1}{2} \sum_{m=0}^l |c_{lm}(t)|^2. \tag{18}$$

The index l will also be referred to as “wavenumber” following the analogy with an expansion in spherical harmonics and plane waves.⁶⁸ We denote the evolution of the basis coefficients by L , where \mathbf{c} is the vector containing all basis coefficients. In particular, the evolution of the magnitude of c_{lm} will be expressed as $L_r(\mathbf{c}, l, m)$. A special feature of our approach is that the time stepping acts on W , while the model is applied in spectral space. In the actual algorithm, the mapping (15) between elements of $\mathfrak{su}(N)$ and their representation as quantized spherical harmonic coefficients is needed for this purpose. Therefore, the operators L and L_r are not required to be explicitly defined or evaluated but serve only to simplify notation.

B. Model formulation and implementation

The kinetic energy spectrum in a statistically stationary state is fully defined by the mean and variance of the magnitudes of the spherical harmonic coefficients. Thus, these values are imposed by adding a mean-reverting forcing to the evolution of the coefficient magnitudes. Forcing the magnitudes of the basis coefficients is pragmatic since these are stationary if the solution is in a statistically steady state, implying few tunable parameters. Mean reversion is realized by adding an Ornstein–Uhlenbeck (OU) process to the evolution of the coefficient magnitude. This way, the reference spectrum can be reproduced in a coarse numerical simulation. It has been shown⁵⁰ that the OU process arises in the governing equations as the continuous-time limit of the 3D-var data assimilation algorithm.⁴⁹ We, thus, propose

$$d|c_{lm}| = L_r(\mathbf{c}, l, m)dt + \frac{1}{\tau_{lm}}(\mu_{lm} - |c_{lm}|)dt + \sigma_{lm}dB_{lm}^t, \tag{19}$$

where the last two terms constitute the data-driven forcing. The values of μ_{lm} , σ_{lm} , and τ_{lm} follow from high-resolution data obtained from a separate off-line simulation. Here, μ_{lm} and τ_{lm} are means and correlation times. From a sequence of solution snapshots, time series is obtained for each of the basis magnitudes $|c_{lm}|$, of which μ_{lm} is the mean value, and τ_{lm} is the characteristic timescale. The relaxation of the forcing is determined by the timescale τ_{lm} . Deviations of $|c_{lm}|$ from the mean μ_{lm} are nudged back in order to reduce the differences. Randomness is introduced via the term dB_{lm}^t , in which B_{lm}^t is a general random process, defined for each pair l, m separately, and serves to obtain a specified variance. The random process can be tailored to fit the measurement data,⁴³ though the common choice is to let dB_{lm}^t be normally distributed with a variance depending on the time step size.⁶⁹ We choose the latter in what follows and include the variance scaling in σ_{lm} . The value of σ_{lm} depends on the sample variance of the time series, on τ_{lm} and on the adopted time step size, and will be specified later in this section.

In the discrete setting, we apply the forcing defined by the OU process in (19) as a correction after time step is completed. This alters a time-advancement step as follows. Starting from the vorticity W^n at time level t^n , a prediction \bar{W}^{n+1} of the vorticity at the next time level is obtained by integrating Eq. (4) over one time step using the algorithm (10). This prediction is, then, projected onto the basis of spherical harmonics to obtain the corresponding basis coefficients $\{\bar{c}_{lm}^{n+1}\}$. Finally, a correction is applied to these coefficients using (19) to obtain $\{c_{lm}^{n+1}\}$, which are then used to construct the vorticity field W^{n+1} at the new time level. We note that the correction is only applied to the magnitude of the basis coefficients.

The correction procedure (19) will be referred to as *nudging*. We distinguish between *deterministic nudging*, using only the deterministic component of the forcing, and *stochastic nudging*, using both the deterministic and the stochastic component. The former is described as

$$|c_{lm}^{n+1}| = |\bar{c}_{lm}^{n+1}| + \frac{\Delta t}{\tau_{lm}} \left(\mu_{lm, \text{det}} - |\bar{c}_{lm}^{n+1}| \right). \tag{20}$$

The stochastic nudge is defined as

$$|c_{lm}^{n+1}| = |\bar{c}_{lm}^{n+1}| + \frac{\Delta t}{\tau_{lm}} \left(\mu_{lm, \text{stoch}} - |\bar{c}_{lm}^{n+1}| \right) + \sigma_{lm} \Delta B_{lm}^n, \tag{21}$$

where ΔB_{lm}^n is drawn from a standard normal distribution for each l, m , and n independently.

C. Forcing parameters

The parameter definitions in the implementation of Eqs. (20) and (21) will now be described. The nudging procedures in Eqs. (20) and (21) can be characterized as a steady-state Kalman–Bucy filter⁷⁰ with prescribed gain $\Delta t / \tau_{lm}$. The value of τ_{lm} is chosen to be constant, similar to steady-state filters. At each time step, the “observation” consists of coefficients for each spherical harmonic mode separately. The deterministic nudging procedure assumes the observation is a fixed value $\mu_{lm, \text{det}}$, whereas the stochastic approach adopts observations as distributed samples. Here, we use $\mathcal{N}(\mu_{lm, \text{stoch}}, \sigma_{lm}^2)$ as distribution and draw independent samples for each l, m, n separately. Thus, the unresolved interactions between different spherical harmonic modes are modeled as linear stochastic processes, independent for each

value of l, m . This approach has been introduced as Fourier domain Kalman filtering.⁵² For low-dimensional systems, it was analyzed in Fourier space^{51,71} and also shown to be feasible for filtering high-dimensional systems. No covariance matrices have to be computed from the data since the unresolved interactions are treated as independent processes, and additionally, the parameters are determined heuristically, which leads to a simple model with few parameters. The model is found to be stable since each coefficient is independently nudged toward a known mean value.

In the continuous formulation (19), τ_{lm} can take on any positive value. In the discrete form (20), (21), τ_{lm} can take on values in the interval of $[\Delta t, \infty)$. For $\tau_{lm} = \Delta t$, the forcing ensures that the magnitude $|c_{lm}|$ of the corresponding coefficient becomes constant in the case of deterministic nudging. In the case of stochastic nudging, this value of τ_{lm} ensures that $|c_{lm}|$ evolves as Gaussian noise with the specified mean and variance. In the limit of large τ_{lm} , the forcing approaches zero and the unforced dynamics is retained.

The nudging procedures in Eqs. (20) and (21) are treated as first-order autoregressive models with drift coefficient $(1 - \Delta t/\tau_{lm})$ and mean $\mu_{lm, \text{stoch}}$, which is a discretization of the OU process (19). The value of τ_{lm} is found by fitting the autocovariance function of the OU process to the sample autocovariance as obtained from the reference high-resolution simulation. The value of τ_{lm} is expected to decrease as larger wavenumbers l are considered. This increases the contribution of the model term to the dynamics of the coefficients c_{lm} at those wavenumbers. Therefore, with increasing spatial resolution, one will resolve finer lengthscales associated with larger l , whose contributions correspond closer and closer to the direct observations. This is in accordance with theoretical results for filter performance.⁵²

The values of σ_{lm} , $\mu_{lm, \text{stoch}}$, and $\mu_{lm, \text{det}}$ are chosen so that the reference energy spectrum is reproduced when the model is applied. Treating $|c_{lm}|$ as a stochastic variable, we observe that $\mathbb{E}(|c_{lm}|^2)$ is the expected energy content of the basis element T_{lm}^N . Through the definition of the variance, we find that

$$\mathbb{E}(|c_{lm}|^2) = \text{var}(|c_{lm}|) + \mathbb{E}(|c_{lm}|)^2. \quad (22)$$

We define σ_{lm} so that variance of the autoregressive model coincides with the sample variance s_{lm}^2 of the reference time series, i.e.,

$$\sigma_{lm} = s_{lm} \sqrt{1 - \left(1 - \frac{\Delta t}{\tau_{lm}}\right)^2}, \quad (23)$$

where s_{lm} is the sample standard deviation of $|c_{lm}|$ as obtained from the high-resolution simulation. To obtain the desired energy content, $\mu_{lm, \text{stoch}}$ is subsequently chosen as $\mathbb{E}(|c_{lm}|)$. In the case of deterministic nudging, the variance of $|c_{lm}|$ vanishes when $\tau_{lm} = \Delta t$. To obtain the desired energy content in this limit, $\mu_{lm, \text{det}}$ is chosen as $\sqrt{\mathbb{E}(|c_{lm}|^2)}$. The mean, variance, and correlation time are estimated using standard unbiased estimators of which the mean squared error decreases linearly with the number of used samples. It is assumed that the mean and variance are constant in time, therefore requiring that the flow is in a statistically steady state.

For each basis function, only three parameters need to be measured: the mean, the variance, and the correlation time. This outlines the simplicity of the model. These parameters are inferred from the data, do not require additional tuning, and are defined up to the

resolution of the reference solution. Furthermore, the basis of spherical harmonics is resolution-independent. Therefore, the forcing parameters only depend on the reference data and not on the choice of the coarse-grid resolution or time step size, implying that the model is self-consistent.⁷² This is further corroborated in Sec. IV B of the paper by applying the model at various low resolutions.

IV. NUMERICAL EXPERIMENTS

In this section, we apply the forcing proposed in Sec. III to coarse numerical simulations. We describe the reference solution and introduce the measured variables that constitute the model data. The forcing is applied at different coarse computational grids using several model configurations. The model results are compared to the reference solution and the no-model coarse numerical solution and are assessed in terms of statistical quantities of the resulting time series of the basis coefficients, in terms of attained vorticity values in physical space, and in terms of inter-scale energy transfer. Finally, we illustrate that the application of the model yields accurate long-time solutions on coarse computational grids.

A. Description of reference solution

The reference solution is acquired from the discretized equations described in Sec. II and adopts a resolution $N = 512$. The initial condition is the smooth vorticity field as shown in the left panel of Fig. 3, which is also adopted in later numerical simulations using lower resolutions. This initial condition is randomly generated and contains only large scales of motion. The initial condition is well resolved on the coarse computational grids, ensuring that any difference with respect to the reference in the obtained solutions is due to coarsening effects and not due to a difference in the initial condition. The vorticity is evolved until $t = 6500$, shown on the right panel of Fig. 3, at which a statistically steady state is reached. This was verified by averaging the kinetic energy spectrum over several time durations. Large-scale structures dominate the statistically steady state due to the formation of energy condensates in the absence of large-scale dissipation.² High-resolution snapshots are collected every time unit after reaching this state. A total of 1000 snapshots is collected to ensure that estimates of the mean, variance, and correlation times are sufficiently accurate.

By projecting the snapshots onto the basis $\{T_{lm}^N\}$, a time series of coefficients for each spherical harmonic mode is obtained. These coefficients are complex-valued; however, in what follows, we will only consider the time series of the corresponding magnitudes since these are the quantities that the proposed model acts on.

The forcing parameters are shown in Fig. 4, sorted per basis coefficient. Here, we show the measured means, standard deviations, and correlation times that are used in the model. On a grid of resolution N , a total of $N(N + 1)/2 - 1$ basis functions T_{lm}^N is available, which can be sorted in ascending order of l and m . Here, only the first 2079 values are shown, corresponding to all resolvable modes for $N = 64$, a coarse resolution that will be investigated momentarily. A decreasing mean value and variance are observed as the scale size is decreased. This is seen until basis functions with $l = 23$ are considered, at the 275th basis coefficient, after which the mean and variance remain roughly constant. This corresponds to the wavenumber at which the reference energy spectrum follows the l^{-1} decay. The measured correlation time τ_{lm} becomes smaller as larger wavenumbers are considered,

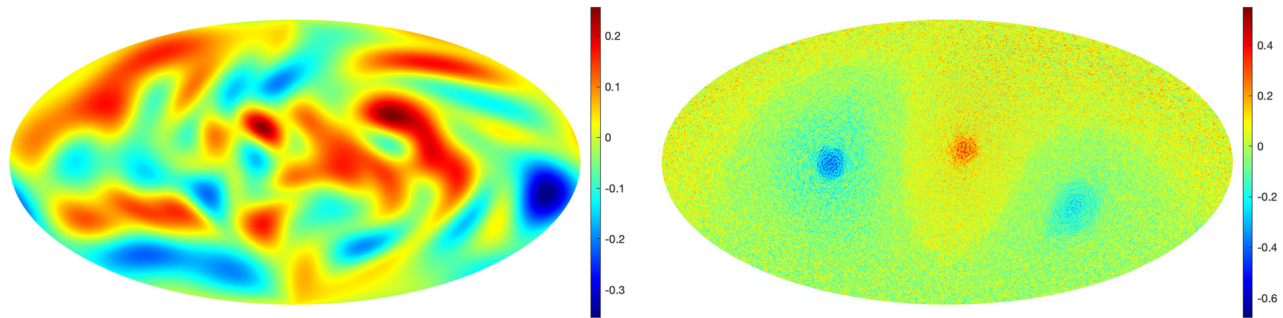


FIG. 3. Left: initial vorticity field used in the numerical simulations performed throughout the paper. Right: snapshot of the vorticity field after reaching a statistically steady state.

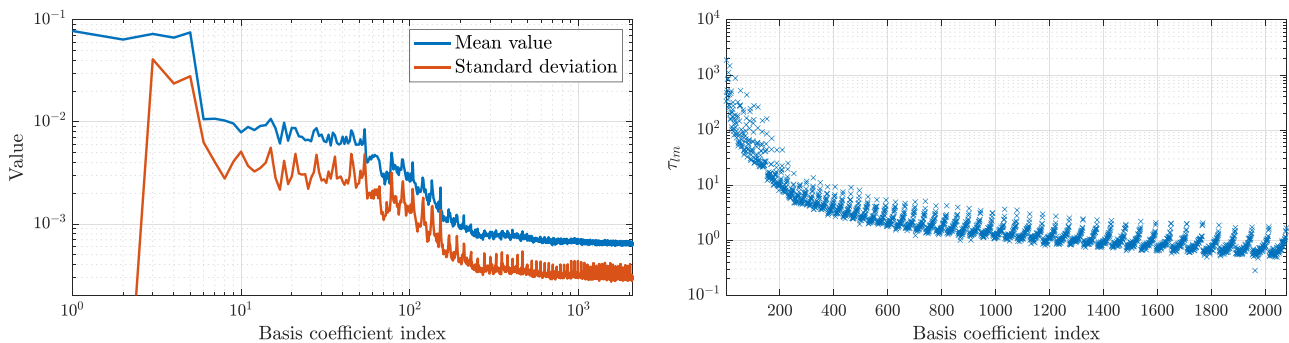


FIG. 4. Left: measured means and standard deviations of the absolute value of each basis coefficient of the reference solution. Right: estimated correlation time for each basis coefficient of the reference solution.

which indicates that the smaller scales in the flow behave in an increasingly dynamic manner. The small values of τ_{lm} result in a relatively larger contribution from the model term to the dynamics of the smallest resolvable scales.

B. Coarse-grid flow simulations

In this subsection, the performance of the model is tested in coarse-grid numerical simulations of the flow. In particular, the model is applied at resolutions $N=64$ and $N=32$ to show that the forcing parameters are applicable at different coarse resolutions. The chosen levels of coarsening provide a significant reduction in computational costs. At the same time, the dominant flow patterns can be accurately resolved, as shown in Sec. II. Four different settings for the model are studied by varying the minimal wavenumber at which the model is activated and by either enabling or disabling the stochastic model term. The scales at which the model is applied are $l \geq 1$ and $l \geq 8$ for resolutions $N=64$ and $N=32$, in order to capture the same flow complexity at different resolutions. The choice of $l \geq 1$ corresponds to applying the model at all available scales, whereas $l \geq 8$ only applies to small-scale flow features. For each resolution, we illustrate the need for modeling by providing snapshots of the filtered reference solution and the no-model coarse-grid solution. From these figures, the qualitative features of the solution at different resolutions become apparent.

We first consider the results at resolution $N=64$. A qualitative comparison of the different numerical solutions is provided in Fig. 5. The top left panel shows a snapshot of the reference solution at the statistically steady state, where the high-frequency components have been filtered from the solution. As before, the applied filter is a spectral cutoff filter where the cutoff wavenumber is defined by the coarse-grid resolution. Coherent large-scale vorticity structures that are resolvable on the coarse grid are visible in this snapshot. The merit of the forcing can be observed through the differences between the coarse numerical simulation results. The top middle panel shows the no-model coarse solution, which shows clear qualitative differences with the reference result. The top right panel and the bottom row show forced coarse numerical solutions at statistically steady states, using the different forcing settings. Evidently, the latter snapshots reveal a smoother vorticity field and a more accurate representation of the reference vorticity, compared to the coarse no-model simulation. In particular, a qualitative agreement in terms of large-scale vortex structures may be observed. In this specific case, a large connected positive vorticity structure (in red) and two smaller negative vorticity structures (in blue) are reproduced when applying the model. Interestingly, the proposed nudging concentrates some additional positive vorticity in the tail of the coherent structure (in red), whereas no such behavior is observed for the negative vorticity.

The qualitative differences are reflected in the energy spectra, visualized in Fig. 6, showing the energy spectra using the forcing for

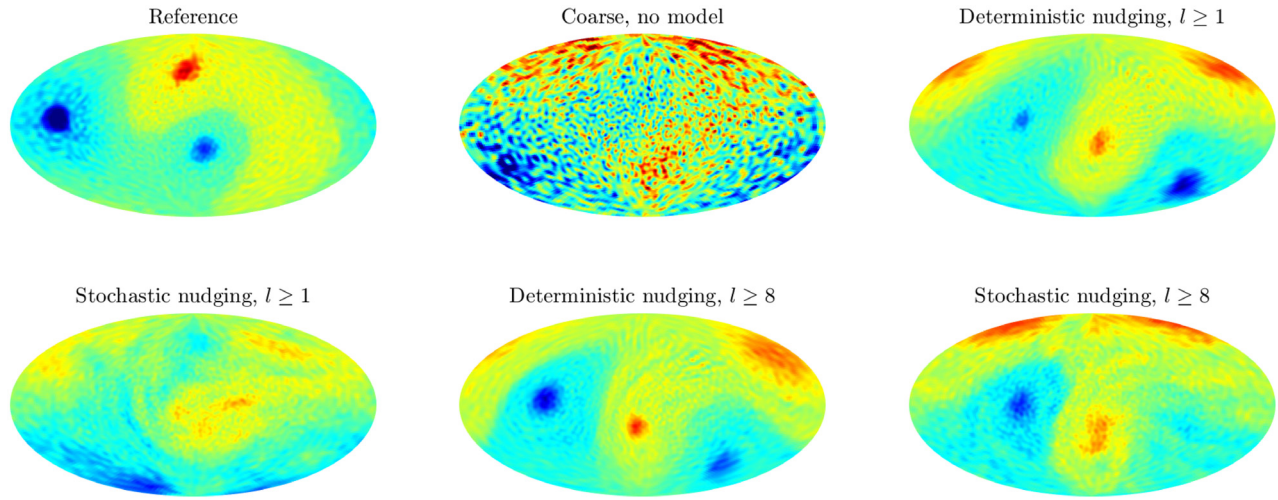


FIG. 5. Snapshots of numerical solutions at a statistically steady state. Top left: filtered reference solution, displaying only modes resolvable for $N = 64$. Top middle: no-model coarse numerical solution. Top right and bottom row: coarse numerical solution with forcing applied, using the full model term or only the deterministic part, with varying minimal wavenumber at which the forcing is applied.

$l \geq 1$ and $l \geq 8$ in the two panels. By construction, nudging reduces the energy content in the small scales of the flow. Accurate energy levels are observed for both the deterministic and stochastic nudging procedures. These results are observed for both choices of scales at which the forcing is applied. A good agreement in the energy at the large scales is observed for all performed simulations. Particularly, the energy spectra demonstrate a striking agreement at the smallest resolved scales when the model is applied. This suggests that the choice of parameters for the deterministic and stochastic forcing is well suited for reproducing the energy spectra at these scales.

A quantitative comparison of the statistics of the solutions is given in Fig. 7. For each basis coefficient, the mean, standard deviation, and estimated correlation time are shown. The mean and the standard

deviations of the time series display similar qualitative behavior regardless of the minimal wavenumber at which the forcing is applied. For these quantities, both the deterministic nudging and the stochastic nudging lead to significant improvement compared to the no-model results. Including the stochastic component of the forcing, based on the high-resolution reference data, leads to an increased agreement at the smaller scales of the flow, indicating that the inclusion of additional variance in the forcing of the small scales leads to a truthful reproduction of these statistical quantities.

The estimated correlation times of the large-scale modes ($l \leq 8$) in Fig. 7 show that deterministic nudging of all modes yields an improved correlation time compared to the no-model case. However, the stochastic nudging procedure for $l \geq 1$ leads to smaller correlation

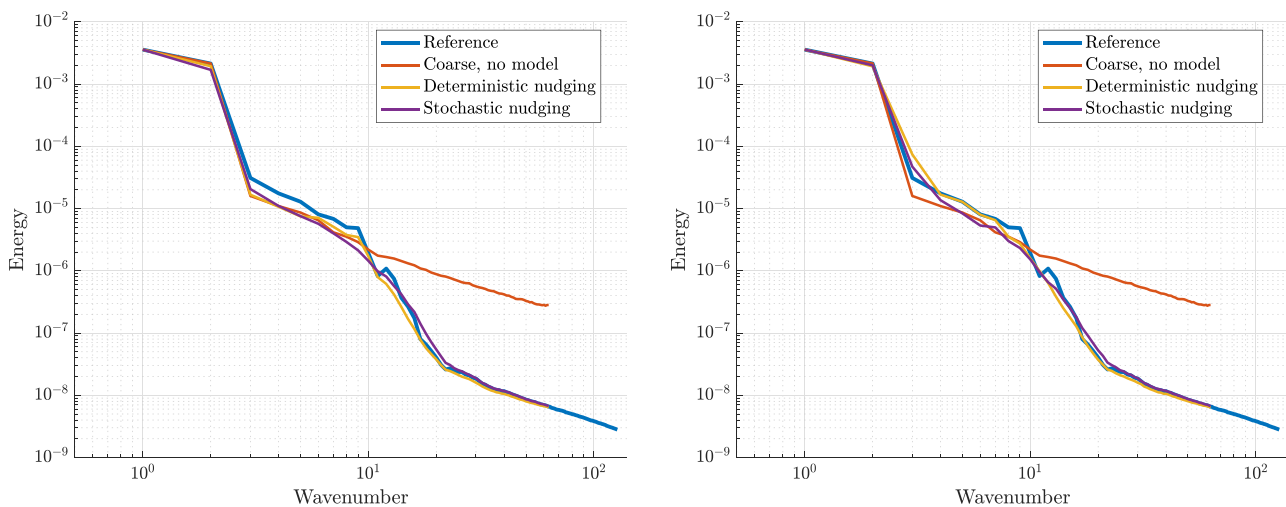


FIG. 6. Average energy spectra for forced coarse solutions, using $N = 64$, compared to the energy spectra of the reference solution and the no-model coarse solution. The forcing is applied at wavenumbers $l \geq 1$ (left) and wavenumbers $l \geq 8$ (right).

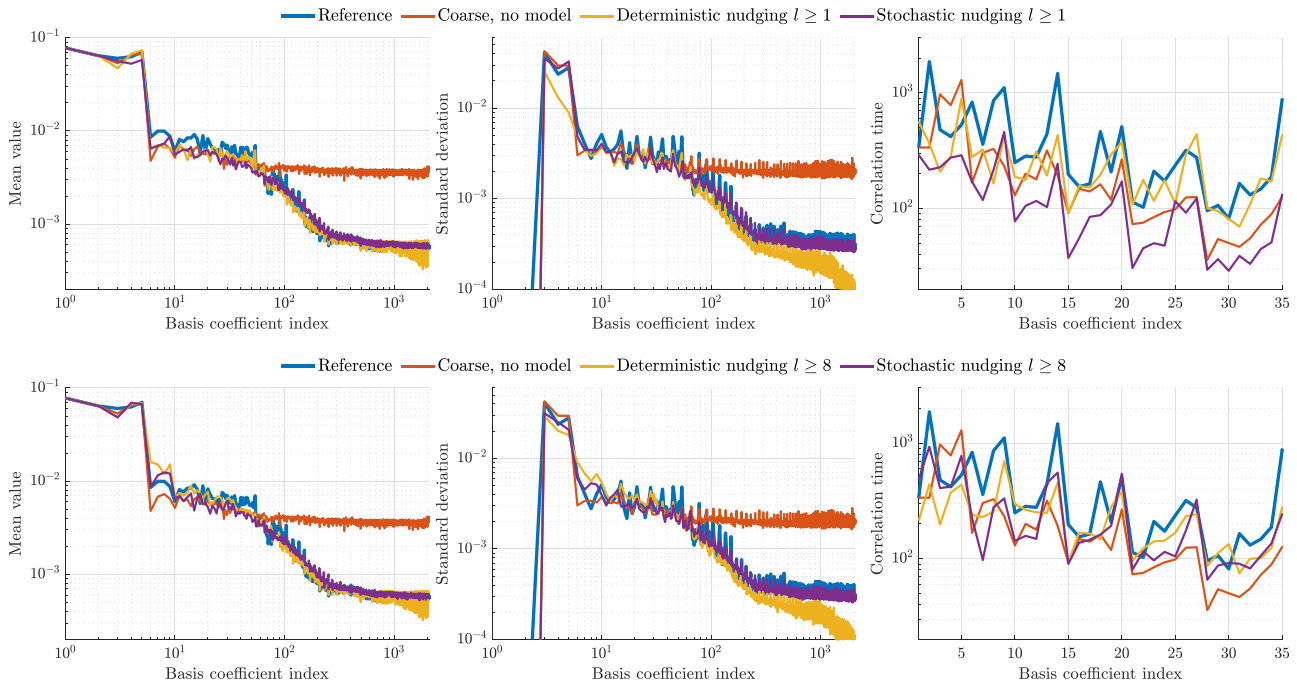


FIG. 7. Statistics of the basis coefficient time series of the reference solution, no-model coarse solution, and coarse solution with the model applied for $N=64$. Shown here are the results when applying the model at wavenumbers $l \geq 1$ (top row) and $l \geq 8$ (bottom row). The mean value (left) and standard deviation (middle) are shown for all wavenumbers. The correlation time (right) is shown for the large-scale components, with wavenumbers $l \leq 8$.

times compared to the coarse no-model simulation, implying that the stochastic component of the forcing is too strong. A qualitative improvement is observed when applying the model to wavenumbers $l \geq 8$, for both deterministic and stochastic nudging. These results suggest that the evolution of large scales in the flow benefits from an accurate statistical description of the evolution of small scales. This coincides with a basic premise underlying large-eddy simulation.

A comparison between the different outcomes in physical space is carried out to gain insight into the predictions of the phases of the basis coefficients. For this purpose, we compare empirical probability distribution functions (pdfs) of attained vorticity values in physical space throughout the simulation. The pdfs are shown in Fig. 8, comparing the nudging procedures applied at wavenumbers $l \geq 1$ and $l \geq 8$ to the reference and no-model simulation at resolution $N=64$. A distribution with two distinct peaks is obtained from the reference,

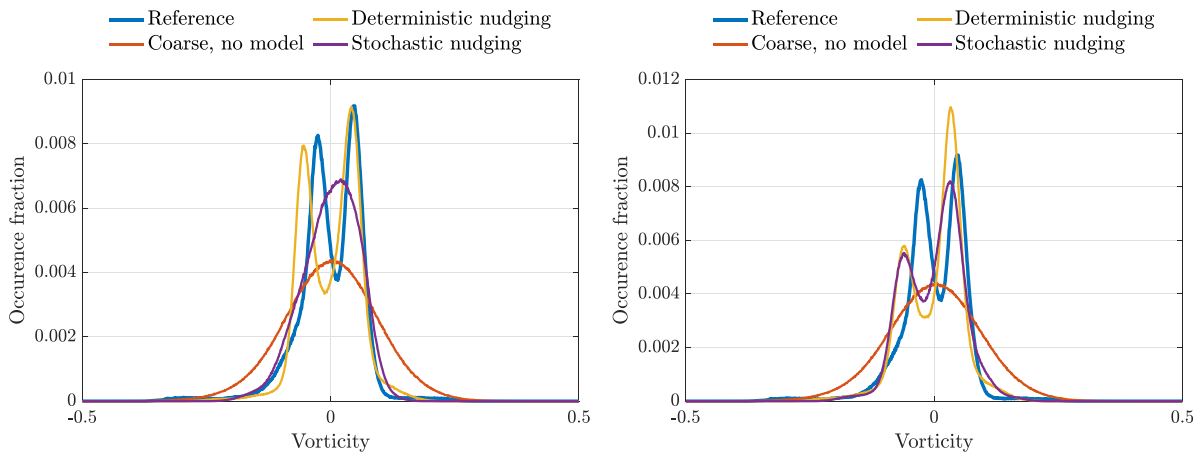


FIG. 8. Probability density functions (pdfs) of the vorticity values. The pdfs of the reference and the no-model coarse ($N=64$) numerical simulation are compared to coarse numerical simulations where deterministic and stochastic nudging are applied at wavenumbers $l \geq 1$ (left) and $l \geq 8$ (right).

where the peaks stem from the large-scale vorticity structures observed in Fig. 5. Despite the no-model simulation yielding a markedly different pdf than the reference, including the deterministic nudging at all wavenumbers leads to an accurate pdf. Stochastic nudging at all wavenumbers leads to a qualitatively different pdf where the peaks distinct peaks are no longer observed. This is attributed to the breakup of the large-scale vorticity structures and indicates that stochastic forcing of the largest scales is undesirable. Notably, an accurate energy spectrum is obtained, but the discrepancy in attained vorticity values implies that phase errors are present. Applying the nudging procedure to wavenumbers $l \geq 8$ leads to an improvement in the pdf for both the deterministic and the stochastic approaches. These results suggest that reducing the energy level in the small-scale components of the flow already leads to qualitatively accurate results, which we attribute to the dominance of the large-scale structures in the reference.

The numerical experiment is repeated at a resolution $N = 32$ to demonstrate that the proposed model yields forcing parameters that can be efficiently applied at different coarse resolutions. At this resolution, large spatial structures in the flow may still be resolved with acceptable accuracy. The forcing will be applied at wavenumbers $l \geq 1$ and $l \geq 8$, where the model affects all scales of motion in the former and only the small scales in the latter.

A qualitative comparison of the statistically steady states is given in Fig. 9. It may be seen that the model effectively produces a smooth vorticity field with qualitatively similar features as the reference solution. This is reflected by the decrease in energy in the smallest resolvable scales compared to the no-model formulation, as shown in the energy spectra in Fig. 10. As previously observed, all coarse-grid numerical simulations accurately capture the energy in the largest scales of motion. Applying the model also leads to a notable agreement with the reference solution in the average energy levels of the smallest resolvable scales.

A comparison of the mean value, standard deviation, and estimated correlation times of the time series of the basis coefficients is given in Fig. 11. Applying the model leads to a clear

improvement in the mean and variance of the coefficients, regardless of the choice of length scales at which the forcing is applied. Employing the deterministic forcing at all lengthscales yields a good agreement in the correlation times, whereas the stochastic forcing reduces the measured correlation times and yields no improvement. The correlation times are also found to improve when applying the deterministic model only to components with wavenumber $l \geq 8$. The stochastic forcing displays no significant improvement when applied at these wavenumbers.

The pdfs of the attained vorticity values in physical space at resolution $N = 32$ are shown in Fig. 12. These results are qualitatively similar to those presented earlier at resolution $N = 64$. A good agreement with the reference is observed when applying deterministic nudging at all wavelengths, whereas stochastic nudging leads to notably different pdf. The latter is attributed to the breakup of large-scale vortices and indicates phase errors in the solution. Both deterministic and stochastic nudging at wavelengths $l \geq 8$ lead to a considerable improvement in the pdfs when compared to the coarse no-model simulation.

C. Average inter-scale energy transfer

The truncation of resolvable scales in coarse numerical simulations often leads to incorrect inter-scale energy transfers.⁷³ The energy rate of change per wavenumber can be explicitly computed via

$$\frac{dE_l}{dt} = \frac{1}{2} \frac{d}{dt} \left(\sum_{m=0}^l c_{lm} c_{lm}^* \right) = \text{Re} \left(\sum_{l=0}^m c_{lm} \dot{c}_{lm}^* \right), \quad (24)$$

where $*$ denotes the complex conjugate, and \dot{c}_{lm} follows from Eq. (16). This energy rate of change depends both on the magnitudes of the basis coefficients and the phases due to the complex conjugation, in contrast to the energy itself which depends solely on the former. Hence, the energy rate of change is not explicitly enforced in the proposed subgrid-scale model. The average rates of change per

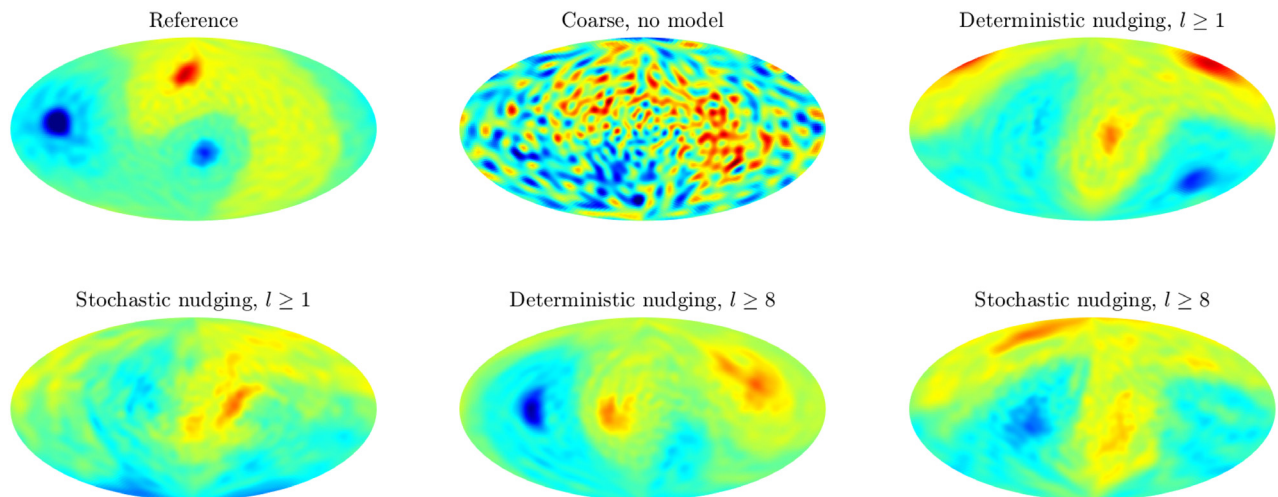


FIG. 9. Snapshots of numerical solutions at a statistically steady state. Top left: filtered reference solution, displaying only modes resolvable for $N = 32$. Top middle: no-model coarse numerical solution. Top right and bottom row: coarse numerical solution with forcing applied, using the full model term or only the deterministic part, with varying minimal wavenumber at which the forcing is applied.

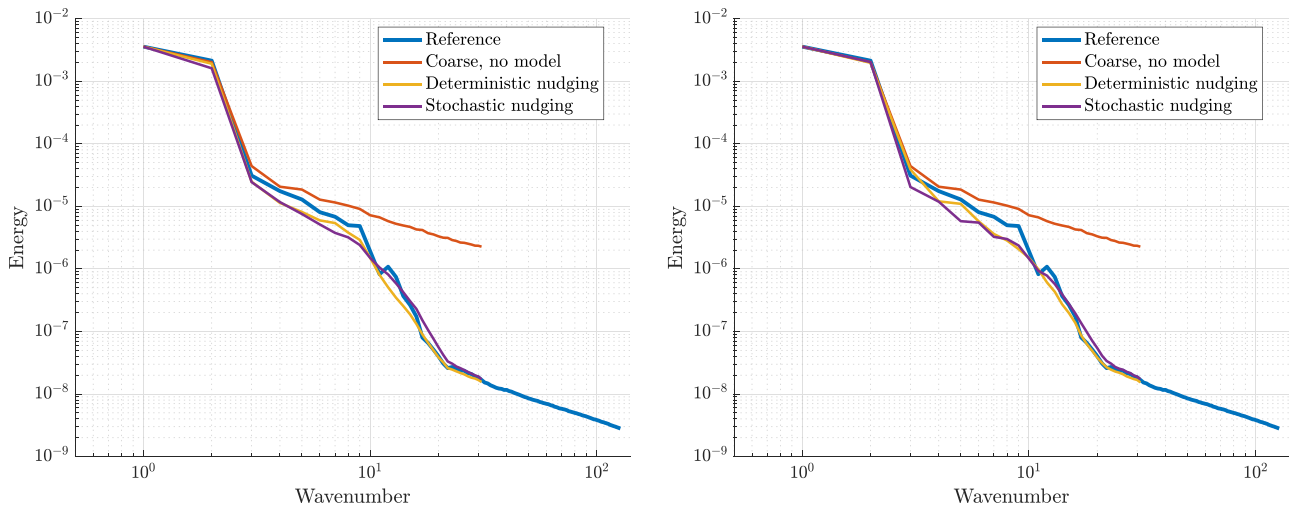


FIG. 10. Average energy spectra for forced coarse solutions, using $N = 32$, compared to the energy spectra of the reference solution and the no-model coarse solution. The forcing is applied at wavenumbers $l \geq 1$ (left) and wavenumbers $l \geq 8$ (right).

wavenumber are shown in Fig. 13 when applying the nudging procedure at wavenumbers $l \geq 8$ at resolutions $N = 64$ and $N = 32$. An improvement in the energy transfer in the smallest resolvable scales observed for $N = 32$ is attributed to a significant improvement in the energy levels at these scales, compared to the no-model results. This improvement is marginal for $N = 64$. No improvement in the energy

transfers at the large scales is observed. These results underpin that imposing additional statistics, such as the energy transfer, may lead to more accurate coarse numerical simulations. Possible ways to achieve this are via a variable forcing strength or constraints on the phases of the basis coefficients, but these fall outside the scope of this paper.

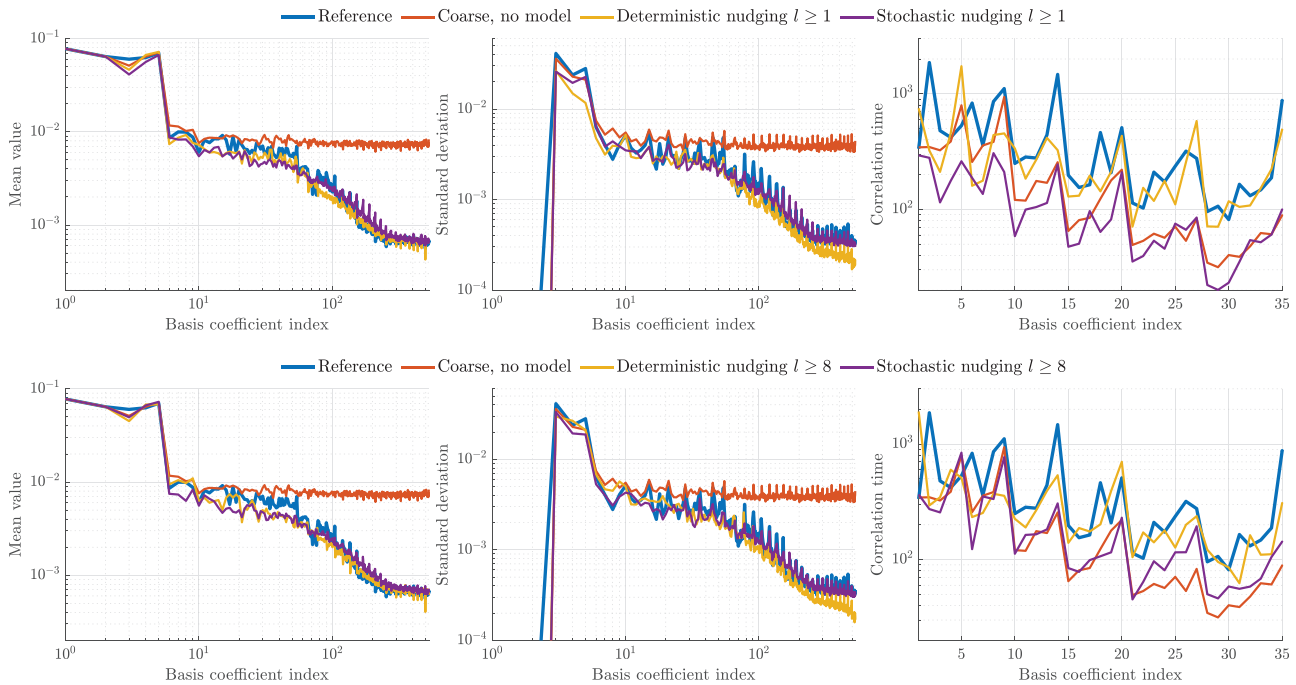


FIG. 11. Statistics of the basis coefficient time series of the reference solution, no-model coarse solution, and coarse solution with the model applied for $N = 32$. Shown here are the results when applying the model at wavenumbers $l \geq 1$ (top row) and $l \geq 8$ (bottom row). The mean value (left) and standard deviation (middle) are shown for all wavenumbers. The correlation time (right) is shown for the large-scale components, with wavenumbers $l \leq 8$.

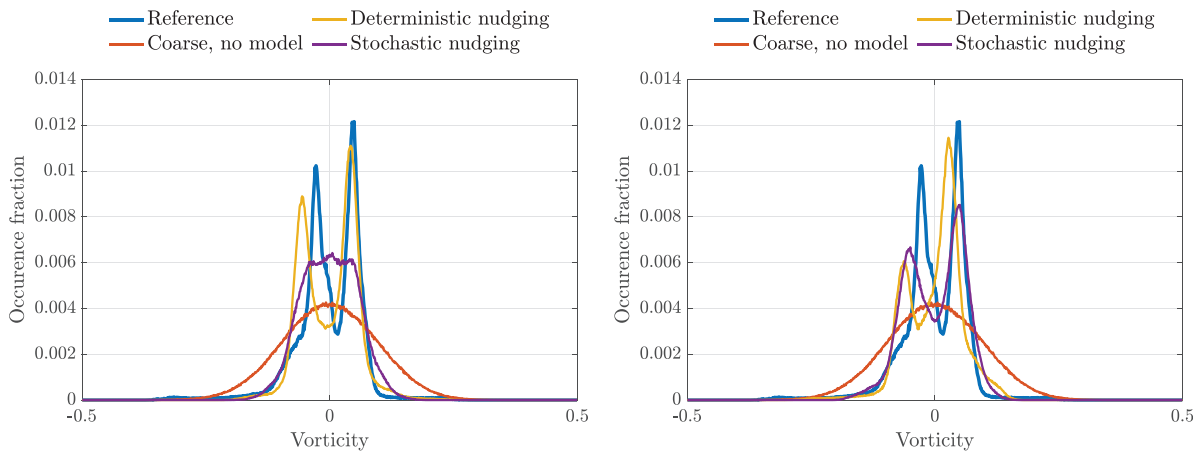


FIG. 12. Probability density functions (pdfs) of the vorticity values. The pdfs of the reference and the no-model coarse ($N = 32$) numerical simulation are compared to coarse numerical simulations where deterministic and stochastic nudging are applied at wavenumbers $l \geq 1$ (left) and $l \geq 8$ (right).

D. Large-scale vortex dynamics at statistically steady states

The qualitative predictions of coarse-grained modeled dynamics can be analyzed by means of the vortex trajectories over long integration times. Here, the vortex movement is tracked by locating the maximum and minimum attained vorticity value at each solution snapshot. High-resolution numerical experiments indicate that the ratio between the angular momentum and enstrophy governs the number of large-scale vortex structures in the final statistically steady state.⁶⁵ This ratio is determined by the initial condition and remains constant throughout the no-model numerical simulations since the angular momentum and the enstrophy are conserved quantities in the discretized system. Additionally, the vortex trajectories are found to be stable. Thus, the long-term qualitative behavior of the coarse numerical solutions can be assessed by measuring the number of large-scale vortices and their

trajectories. As we previously observed, the coarse-grained modeled vorticity fields show qualitative agreement in terms of the number of vortices. Here, we demonstrate the capability of the model to accurately yield stable long-time vortex dynamics by tracking vortex movement over long simulation times.

The long-time vortex trajectories for various numerical realizations are shown in Fig. 14. The reference trajectories are obtained from the high-resolution simulation as used in Sec. IV A. The model results at resolutions $N = 32$ and $N = 64$ are obtained by applying the model to wavenumbers $l \geq 8$. The reference trajectories display stable movement along clearly defined trajectories about a fixed axis. Such behavior is not observed for the coarse no-model results, where instead the extreme values of the vorticity move in a seemingly unorganized fashion without distinct trajectories. Applying the model to either of the presented resolutions yields a noticeable qualitative improvement in the measured vortex movement. In particular, we

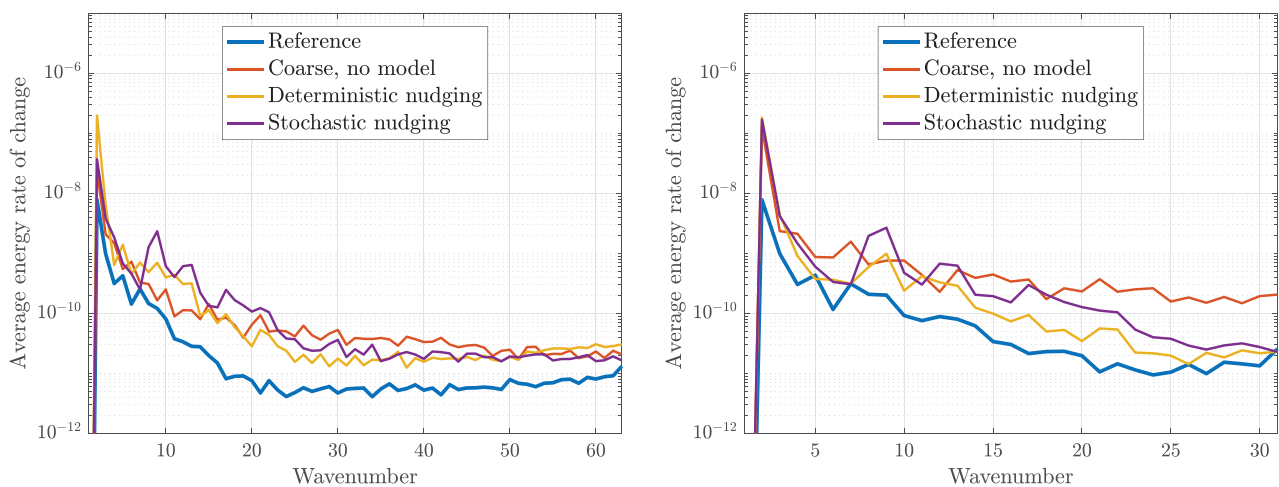


FIG. 13. Average energy rate of change per wavenumber. The reference and coarse no-model simulations are compared to deterministic nudging and stochastic nudging at resolutions $N = 64$ (left) and $N = 32$ (right). The results in this figure are obtained when nudging at wavenumbers $l \geq 8$.

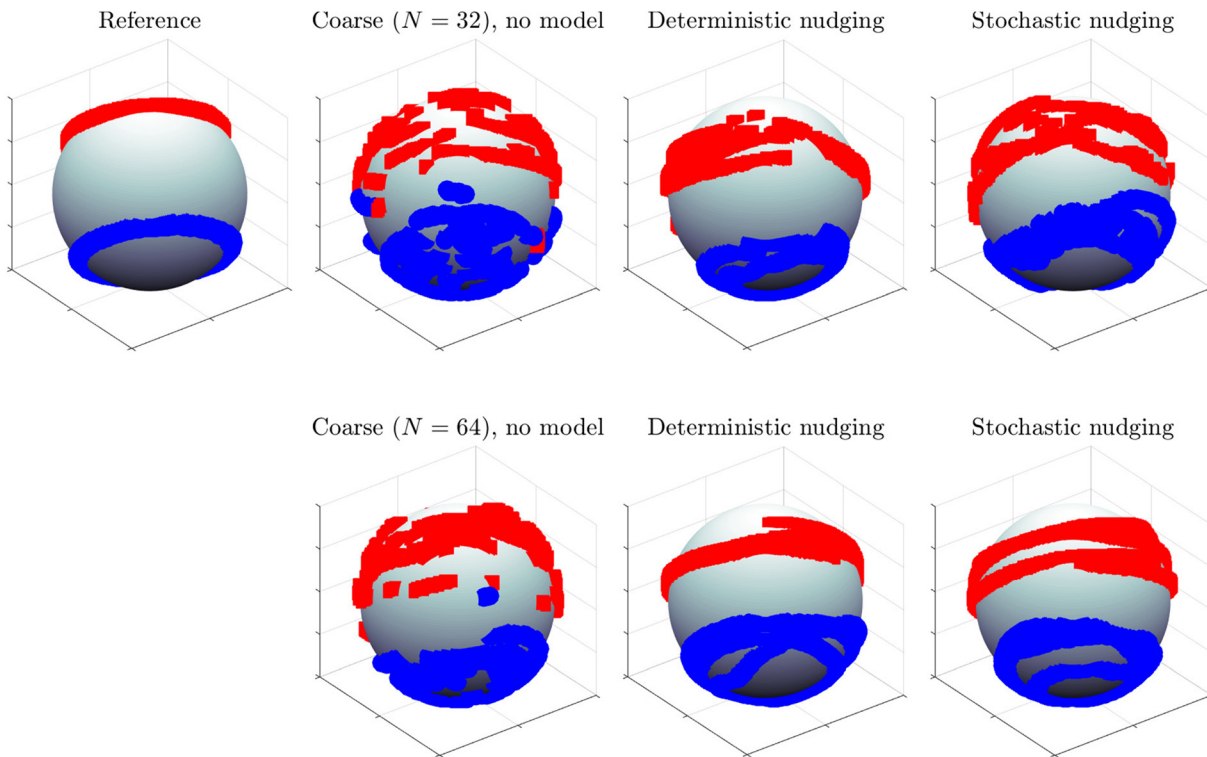


FIG. 14. Trajectories of large-scale vortices for various numerical solutions. The red and blue lines denote the trajectories of the maximum and minimum vorticity values, respectively. Shown are the measured trajectories of the reference solution (top left). The coarse no-model numerical solution and the coarse solution with the model at resolution $N=32$ are displayed on the top row. Both the deterministic and the stochastic models are applied to wavenumbers $l \geq 8$ at this resolution. The bottom row shows the realizations at resolution $N=64$, where the model is applied to wavenumbers $l \geq 8$.

identify trajectories about the same fixed axis as the reference trajectories, but the model trajectories exhibit perturbations. The perturbations appear stronger when stochastic nudging is applied and when coarser grids are considered.

V. CONCLUSIONS AND OUTLOOK

In this paper, we have proposed and assessed a standalone data-driven model for the coarsening of the Euler equations on the sphere. High-resolution simulation snapshots were used as a reference. These data were decomposed into spherical harmonic modes, and corresponding time series of coefficients were determined. A stochastic model was introduced to compensate for shortcomings introduced by severe coarsening. The model parameters were obtained from statistics of the spherical harmonic coefficients time series. In particular, the proposed model was designed to reproduce the kinetic energy spectrum of the reference data in statistically steady states by adopting a nudging strategy similar to continuous data assimilation.

The model is imposed using a prediction–correction scheme leading to a formulation similar to a steady-state Fourier domain Kalman filter. We opted for a separate nudging strength for each of the forced lengthscales, dependent on the corresponding measured characteristic timescale, and demonstrated that this approach accurately recovers the energy levels in small resolved spatial scales and leads to stable long-time solutions. Moreover, no assumptions about

the employed resolution are used in the derivation model. This was demonstrated by first measuring the forcing parameters and subsequently applying the model on several coarse computational grids. The proposed stochastic and deterministic models were not found to differ much in terms of results in spectral space. Both approaches yielded accurate kinetic energy spectra at strong coarsening. In addition, the deterministic model yielded accurate correlation times of the magnitudes of the spherical harmonic basis coefficients, indicating accurate evolution of the large-scale flow features. Observations in physical space revealed that the stochastic forcing of large scales yielded phase errors in the solution.

The results in this paper show that the decomposition of a high-resolution reference signal into spatial global basis functions and temporal coefficients can be employed efficiently to obtain resolution-independent forcing parameters to be used in models for coarse numerical simulations. The proposed model relies on several simplifying assumptions, which will be scrutinized in future work. In particular, the robustness of the model in terms of stability and accuracy with respect to varying nudging strengths will be assessed and constraints based on inter-scale energy transfers may be imposed. The connection to data assimilation algorithms and Kalman filtering theory may help to extend the model and weaken underlying assumptions, for example by including estimated covariance between different spherical harmonic modes in the model.

The approach presented here is general for flows in statistically stationary states and is not restricted to the two-dimensional Euler equations or the use of spherical harmonic modes as a global basis. Different flow settings may be considered by adopting, for example, a Fourier basis for periodic domains⁷⁴ or, more generally, proper orthogonal decomposition (POD) modes when boundaries are present in the domain.⁶⁷ Extensions to spatially and temporally correlated forcing can be considered as well using spectral POD (SPOD).^{75–77} Further work will be dedicated to extending the proposed model to different sophisticated flow settings, such as Kraichnan turbulence, two-dimensional Rayleigh–Bénard convection, the rotating Euler equations on the sphere, or the quasi-geostrophic equations on the sphere.

ACKNOWLEDGMENTS

The authors would like to thank Darryl Holm, at the Department of Mathematics, Imperial College London, Erwin Luesink and Arnout Franken, at the University of Twente, and Klas Modin, at Chalmers University of Technology, for their valuable input and discussions in the context of the SPRESTO project, funded by the Dutch Science Foundation (NWO) in their TOP1 program.

AUTHOR DECLARATIONS

Conflict of Interest

The authors have no conflicts to disclose.

Author Contributions

Sagy Ephrati: Investigation (equal); Methodology (equal); Software (equal); Writing – original draft (equal). **Paolo Cifani:** Methodology (equal); Software (lead); Supervision (equal); Writing – review & editing (equal). **Milo Viviani:** Methodology (equal); Software (equal); Writing – review & editing (equal). **Bernard J. Geurts:** Funding acquisition (equal); Supervision (equal); Writing – review & editing (equal).

DATA AVAILABILITY

The data that support the findings of this study are available from the corresponding author upon reasonable request.

REFERENCES

- V. Zeitlin, *Geophysical Fluid Dynamics: Understanding (Almost) Everything with Rotating Shallow Water Models* (Oxford University Press, 2018).
- M. Chertkov, C. Connaughton, I. Kolokolov, and V. Lebedev, “Dynamics of energy condensation in two-dimensional turbulence,” *Phys. Rev. Lett.* **99**, 084501 (2007).
- G. Boffetta and R. E. Ecke, “Two-dimensional turbulence,” *Annu. Rev. Fluid Mech.* **44**, 427–451 (2012).
- G. D. Nastrom, K. S. Gage, and W. H. Jasperson, “Kinetic energy spectrum of large- and mesoscale atmospheric processes,” *Nature* **310**, 36–38 (1984).
- E. Luesink, “Stochastic geometric mechanics of thermal ocean dynamics,” Ph.D. thesis, Imperial College London, 2021.
- F. Bos and B. J. Geurts, “Computational error-analysis of a discontinuous Galerkin discretization applied to large-eddy simulation of homogeneous turbulence,” *Comput. Methods Appl. Mech. Eng.* **199**, 903–915 (2010).
- B. Geurts, *Direct and Large-Eddy simulation*, De Gruyter-Computational Science and Engineering (De Gruyter, 2022).
- A. Beck, D. Flad, and C.-D. Munz, “Deep neural networks for data-driven LES closure models,” *J. Comput. Phys.* **398**, 108910 (2019).
- B. Nadiga and D. Livescu, “Instability of the perfect subgrid model in implicit-filtering large eddy simulation of geostrophic turbulence,” *Phys. Rev. E* **75**, 046303 (2007).
- B. J. Geurts, *Elements of Direct and Large Eddy Simulation* (RT Edwards, Inc., 2003).
- P. Sagaut, *Large Eddy Simulation for Incompressible Flows: An Introduction* (Springer Science & Business Media, 2006).
- B. J. Geurts and D. Holm, “Alpha-modeling strategy for LES of turbulent mixing,” in *Turbulent Flow Computation* (Springer, 2002), pp. 237–278.
- U. Piomelli, A. Rouhi, and B. J. Geurts, “A grid-independent length scale for large-eddy simulations,” *J. Fluid Mech.* **766**, 499–527 (2015).
- A. Rouhi, U. Piomelli, and B. Geurts, “Dynamic subfilter-scale stress model for large-eddy simulations,” *Phys. Rev. Fluids* **1**, 044401 (2016).
- F. F. Grinstein, L. G. Margolin, and W. J. Rider, *Implicit Large Eddy Simulation* (Cambridge University Press, Cambridge, 2007), Vol. 10.
- L. G. Margolin and W. J. Rider, “A rationale for implicit turbulence modelling,” *Int. J. Numer. Methods Fluids* **39**, 821–841 (2002).
- R. Moura, J. Peiró, and S. Sherwin, “Under-resolved DNS of non-trivial turbulent boundary layers via spectral/hp CG schemes,” in *Direct and Large Eddy Simulation XII* (Springer, 2020), pp. 389–395.
- G. Mengaldo, D. Moxey, M. Turner, R. C. Moura, A. Jassim, M. Taylor, J. Peiro, and S. Sherwin, “Industry-relevant implicit large-eddy simulation of a high-performance road car via spectral/hp element methods,” *SIAM Rev.* **63**, 723–755 (2021).
- G. Mengaldo, R. Moura, B. Giralda, J. Peiró, and S. Sherwin, “Spatial eigensolution analysis of discontinuous Galerkin schemes with practical insights for under-resolved computations and implicit LES,” *Comput. Fluids* **169**, 349–364 (2018).
- R. Moura, L. Fernandes, A. Silva, G. Mengaldo, and S. Sherwin, “Spectral/hp element methods’ linear mechanism of (apparent) energy transfer in Fourier space: Insights into dispersion analysis for implicit LES,” *J. Comput. Phys.* **471**, 111613 (2022).
- M. A. Mendez, A. Ianiro, B. R. Noack, and S. L. Brunton, *Data-Driven Fluid Mechanics: Combining First Principles and Machine Learning* (Cambridge University Press, 2023).
- M. Kurz, P. Offenhäuser, and A. Beck, “Deep reinforcement learning for turbulence modeling in large eddy simulations,” *Int. J. Heat Fluid Flow* **99**, 109094 (2023).
- C. Xie, J. Wang, and E. Weinan, “Modeling subgrid-scale forces by spatial artificial neural networks in large eddy simulation of turbulence,” *Phys. Rev. Fluids* **5**, 054606 (2020).
- W. Edeling and D. Crommelin, “Reducing data-driven dynamical subgrid scale models by physical constraints,” *Comput. Fluids* **201**, 104470 (2020).
- M. Cao and A. Roberts, “Multiscale modelling couples patches of non-linear wave-like simulations,” *IMA J. Appl. Math.* **81**, 228–254 (2016).
- J. E. Bunder, J. Divahar, I. G. Kevrekidis, T. W. Mattner, and A. J. Roberts, “Large-scale simulation of shallow water waves via computation only on small staggered patches,” *Int. J. Numer. Methods Fluids* **93**, 953–977 (2021).
- J. Divahar, A. Roberts, T. W. Mattner, J. Bunder, and I. G. Kevrekidis, “Two novel families of multiscale staggered patch schemes efficiently simulate large-scale, weakly damped, linear waves,” *Comput. Methods Appl. Mech. Eng.* **413**, 116133 (2023).
- S. R. Ephrati, E. Luesink, G. Wimmer, P. Cifani, and B. J. Geurts, “Computational modeling for high-fidelity coarsening of shallow water equations based on subgrid data,” *Multiscale Model. Simul.* **20**, 1468–1489 (2022).
- M. Altaf, E. Titi, T. Gebrael, O. Knio, L. Zhao, M. McCabe, and I. Hoteit, “Downscaling the 2d Bénard convection equations using continuous data assimilation,” *Comput. Geosci.* **21**, 393–410 (2017).
- J. Charney, M. Halem, and R. Jastrow, “Use of incomplete historical data to infer the present state of the atmosphere,” *J. Atmos. Sci.* **26**, 1160–1163 (1969).
- R. Daley, *Atmospheric Data Analysis* (Cambridge University Press, 1993), Vol. 2.
- A. Azouani, E. Olson, and E. S. Titi, “Continuous data assimilation using general interpolant observables,” *J. Nonlinear Sci.* **24**, 277–304 (2014).

- ³⁵M. Gesho, E. Olson, and E. S. Titi, “A computational study of a data assimilation algorithm for the two-dimensional Navier-Stokes equations,” *Commun. Comput. Phys.* **19**, 1094–1110 (2016).
- ³⁴C. Zerfas, L. G. Rebholz, M. Schneier, and T. Iliescu, “Continuous data assimilation reduced order models of fluid flow,” *Comput. Methods Appl. Mech. Eng.* **357**, 112596 (2019).
- ³⁵R. Maulik, V. Rao, J. Wang, G. Mengaldo, E. Constantinescu, B. Lusch, P. Balaprakash, I. Foster, and R. Kotamarthi, “Efficient high-dimensional variational data assimilation with machine-learned reduced-order models,” *Geosci. Model Dev.* **15**, 3433–3445 (2022).
- ³⁶B. Geurts and F. van der Bos, “Numerically induced high-pass dynamics in large-eddy simulation,” *Phys. Fluids* **17**, 125103 (2005).
- ³⁷T. Palmer, “Stochastic weather and climate models,” *Nat. Rev. Phys.* **1**, 463–471 (2019).
- ³⁸H. Arnold, I. Moroz, and T. Palmer, “Stochastic parametrizations and model uncertainty in the Lorenz’96 system,” *Philos. Trans. R. Soc., A* **371**, 20110479 (2013).
- ³⁹D. Faranda, Y. Sato, B. Saint-Michel, C. Wiertel, V. Padilla, B. Dubrulle, and F. Daviaud, “Stochastic chaos in a turbulent swirling flow,” *Phys. Rev. Lett.* **119**, 014502 (2017).
- ⁴⁰A. Gualandi, D. Faranda, C. Marone, M. Cocco, and G. Mengaldo, “Deterministic and stochastic chaos characterize laboratory earthquakes,” *Earth Planet. Sci. Lett.* **604**, 117995 (2023).
- ⁴¹B. J. Geurts, D. D. Holm, and E. Luesink, “Lyapunov exponents of two stochastic Lorenz 63 systems,” *J. Stat. Phys.* **179**, 1343–1365 (2020).
- ⁴²C. Cotter, D. Crisan, D. D. Holm, W. Pan, and I. Shevchenko, “Numerically modeling stochastic lie transport in fluid dynamics,” *Multiscale Model. Simul.* **17**, 192–232 (2019).
- ⁴³S. R. Ephrati, P. Cifani, E. Luesink, and B. J. Geurts, “Data-driven stochastic lie transport modelling of the 2d Euler equations,” *J. Adv. Model. Earth Syst.* **15**, e2022MS003268 (2023).
- ⁴⁴P. Cifani, S. Ephrati, and M. Viviani, “Sparse-stochastic model reduction for 2d Euler equations,” [arXiv:2301.06326](https://arxiv.org/abs/2301.06326) (2023).
- ⁴⁵D. D. Holm, “Variational principles for stochastic fluid dynamics,” *Proc. R. Soc. London, Ser. A* **471**, 20140963 (2015).
- ⁴⁶V. Resseguier, W. Pan, and B. Fox-Kemper, “Data-driven versus self-similar parameterizations for stochastic advection by lie transport and location uncertainty,” *Nonlinear Processes Geophys.* **27**, 209–234 (2020).
- ⁴⁷R. Brecht, L. Li, W. Bauer, and E. Mémin, “Rotating shallow water flow under location uncertainty with a structure-preserving discretization,” *J. Adv. Model. Earth Syst.* **13**, e2021MS002492 (2021).
- ⁴⁸J. S. Frederiksen and S. M. Kepert, “Dynamical subgrid-scale parameterizations from direct numerical simulations,” *J. Atmos. Sci.* **63**, 3006–3019 (2006).
- ⁴⁹P. Courtier, E. Andersson, W. Heckley, D. Vasiljevic, M. Hamrud, A. Hollingsworth, F. Rabier, M. Fisher, and J. Pailleux, “The ECMWF implementation of three-dimensional variational assimilation (3D-Var). I: Formulation,” *Q. J. R. Meteorol. Soc.* **124**, 1783–1807 (1998).
- ⁵⁰D. Blömker, K. Law, A. M. Stuart, and K. C. Zygalakis, “Accuracy and stability of the continuous-time 3DVAR filter for the Navier–Stokes equation,” *Nonlinearity* **26**, 2193 (2013).
- ⁵¹J. Harlim and A. Majda, “Filtering nonlinear dynamical systems with linear stochastic models,” *Nonlinearity* **21**, 1281 (2008).
- ⁵²A. J. Majda and J. Harlim, *Filtering Complex Turbulent Systems* (Cambridge University Press, 2012).
- ⁵³D. D. Holm, E. Luesink, and W. Pan, “Stochastic mesoscale circulation dynamics in the thermal ocean,” *Phys. Fluids* **33**, 046603 (2021).
- ⁵⁴A. Franken, M. Caliaro, P. Cifani, and B. Geurts, “Zeitlin truncation of a shallow water quasi-geostrophic model for planetary flow,” [arXiv:2306.15481](https://arxiv.org/abs/2306.15481) (2023).
- ⁵⁵J. Marsden and A. Weinstein, “Coadjoint orbits, vortices, and clebsch variables for incompressible fluids,” *Physica D* **7**, 305–323 (1983).
- ⁵⁶V. Zeitlin, “Finite-mode analogs of 2d ideal hydrodynamics: Coadjoint orbits and local canonical structure,” *Physica D* **49**, 353–362 (1991).
- ⁵⁷V. Zeitlin, “Self-consistent finite-mode approximations for the hydrodynamics of an incompressible fluid on nonrotating and rotating spheres,” *Phys. Rev. Lett.* **93**, 264501 (2004).
- ⁵⁸J. Hoppe, “Diffeomorphism groups, quantization, and $\mathfrak{su}(\infty)$,” *Int. J. Mod. Phys. A* **4**, 5235–5248 (1989).
- ⁵⁹M. Bordemann, E. Meinrenken, and M. Schlichenmaier, “Toeplitz quantization of Kähler manifolds and $\mathfrak{gl}(n)$, $n \rightarrow \infty$ limits,” *Commun. Math. Phys.* **165**, 281–296 (1994).
- ⁶⁰M. Bordemann, J. Hoppe, P. Schaller, and M. Schlichenmaier, “ $\mathfrak{gl}(\infty)$ and geometric quantization,” *Commun. Math. Phys.* **138**, 209–244 (1991).
- ⁶¹P. Cifani, M. Viviani, and K. Modin, “An efficient geometric method for incompressible hydrodynamics on the sphere,” *J. Comput. Phys.* **473**, 111772 (2023).
- ⁶²R. I. McLachlan, “Explicit lie-Poisson integration and the Euler equations,” *Phys. Rev. Lett.* **71**, 3043 (1993).
- ⁶³J. Hoppe and S.-T. Yau, “Some properties of matrix harmonics on S^2 ,” *Commun. Math. Phys.* **195**, 67–77 (1998).
- ⁶⁴M. Viviani, “A minimal-variable symplectic method for isospectral flows,” *BIT Numer. Math.* **60**, 741–758 (2020).
- ⁶⁵K. Modin and M. Viviani, “A Casimir preserving scheme for long-time simulation of spherical ideal hydrodynamics,” *J. Fluid Mech.* **884**, A22 (2020).
- ⁶⁶K. Modin and M. Viviani, “Canonical scale separation in two-dimensional incompressible hydrodynamics,” *J. Fluid Mech.* **943**, A36 (2022).
- ⁶⁷S. Ephrati, P. Cifani, and B. Geurts, “Stochastic data-driven pod-based modeling for high-fidelity coarsening of two-dimensional Rayleigh–Bénard turbulence,” in *13th ERCOFTAC Workshop on Direct & Large Eddy Simulation 2022* (ERCOFTAC, 2022).
- ⁶⁸R. Mehrem, “The plane wave expansion, infinite integrals and identities involving spherical Bessel functions,” *Appl. Math. Comput.* **217**, 5360–5365 (2011).
- ⁶⁹D. J. Higham, “An algorithmic introduction to numerical simulation of stochastic differential equations,” *SIAM Rev.* **43**, 525–546 (2001).
- ⁷⁰M. S. Grewal and A. P. Andrews, *Kalman Filtering: Theory and Practice with MATLAB* (John Wiley & Sons, 2014).
- ⁷¹E. Castronovo, J. Harlim, and A. J. Majda, “Mathematical test criteria for filtering complex systems: Plentiful observations,” *J. Comput. Phys.* **227**, 3678–3714 (2008).
- ⁷²J. S. Frederiksen, V. Kitsios, T. J. O’Kane, and M. J. Zidikheri, “Stochastic subgrid modelling for geophysical and three-dimensional turbulence,” in *Nonlinear and Stochastic Climate Dynamics* (Cambridge University Press, 2017), pp. 241–275.
- ⁷³J. Thuburn, J. Kent, and N. Wood, “Cascades, backscatter and conservation in numerical models of two-dimensional turbulence,” *Q. J. R. Meteorol. Soc.* **140**, 626–638 (2014).
- ⁷⁴S. Ephrati, P. Cifani, and B. Geurts, “Data-driven spectral turbulence modeling for Rayleigh–Bénard convection,” [arXiv:2305.10043](https://arxiv.org/abs/2305.10043) (2023).
- ⁷⁵A. Towne, O. T. Schmidt, and T. Colonius, “Spectral proper orthogonal decomposition and its relationship to dynamic mode decomposition and resolvent analysis,” *J. Fluid Mech.* **847**, 821–867 (2018).
- ⁷⁶A. Lario, R. Maulik, O. T. Schmidt, G. Rozza, and G. Mengaldo, “Neural-network learning of SPOD latent dynamics,” *J. Comput. Phys.* **468**, 111475 (2022).
- ⁷⁷O. T. Schmidt, G. Mengaldo, G. Balsamo, and N. P. Wedi, “Spectral empirical orthogonal function analysis of weather and climate data,” *Mon. Weather Rev.* **147**, 2979–2995 (2019).